Mild hybridisation of turboprop engine with high-power-density integrated electric drives

Yuzheng Chen, Tao Yang, IEEE Senior Member, Muhammad Khowja, Antonino La Rocca, Usman Nasir, Shajjad Chowdhury, Dean Evans, Dafydd Kember, Thomas Klonowski, Yohan Arnaud, Lucie Apostin, Thierry Liger, Grégory Cossart, Gaurang Vakil, Chris Gerada, Serhiy Bozhko, *IEEE* Senior Member, Sebastien Detry, Christophe Diette, Patrick Wheeler, IEEE Fellow

***Abstract*—This paper shares with the aerospace community a case study of turboprop mild hybridisation using a recently developed integrated drive system in the University of Nottingham, UK, within the ACHIEVE project under EU H2020 CleanSky 2 program (project No. 737814). The developed drive system enables green taxiing of a turboprop aircraft while on the ground with its engine off, and as an electrical generator when the turboprop is in the air. The entire system is designed to be able to integrate within the power auxiliary gear box (PAGB) of a turboprop aircraft. Some of the key features of the developed system include a high-speed permanent magnet machine (up to 14,200rpm) with dual three-phase design, SiC-based high power density (11.8kW/L for the power converter, 35.3kW/L and 7.2kW/kg for the machine active parts), integrated cooling design for high-temperature operation (>130ºC ambient temperature), fault tolerance consideration with dual channel operation capabilities and sensorless control for entire operational conditions. This paper is giving an overview of the design process of the electrical machine, power converters, and its cooling of the entire drive. Numerical analysis (FEM and CFD) and some experimental results are presented to demonstrate the effectiveness and the desired performance of the developed integrated drive system.**

***Index Terms*— dual three-phase machine, mild-hybridisation, permanent magnet machine, sensorless control, SiC power conversion, turboprop aircraft**

I. Introduction

More electric aircraft (MEA) is a major trend for future aircraft due to its high efficiency, high availability, low CO_2 emission and low noise characteristics. Many functions, which used to be driven by hydraulic, pneumatic and mechanical power, will be replaced with electrical subsystems on board MEA [1]–[4]. In addition, with the increasing of electrical loads on MEA, efficient load management is also a popular research point to avoid the generator overdesign and downsize the overall power system [5], [6]. For a conventional aircraft, the engine is normally started from a gas starter which is supplied by the aircraft auxiliary power unit. Recent advance in electrical machine and power electronics has enabled potentiality of starting engine electrically. Within the EU CleanSky 2 ACHIEVE project (No. 737814), a new high-power-density integrated electric drive system for mild hybridization of turboprop engines has been developed in the University of Nottingham. The developed system is integrated within the power auxiliary gear box (PAGB) of a turboprop aircraft as shown in Fig. 1. This integrated motor/generator (M/G) drive allows multiple functions of green taxiing (when it runs as a motor when aircraft is on ground) and electrical power generation (it runs as a generator when aircraft is in the air). In green-taxiing motoring mode, the integrated drive is powered by a 540V DC bus and can drive propeller from stop status to ground idle speed. Once the engine has started, the integrated drive works as a generation system and feeds into 540V DC bus at least 20kW power.

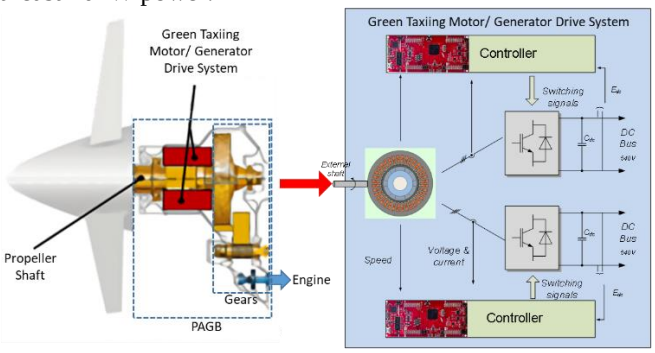

Fig. 1. Green-taxiing motor-generator (M/G) installed in turboprop PAGB.

As shown in Fig. 1, a dual three-phase permanent magnet synchronous machine (PMSM) has been designed with each three-phase channel is feeding one AC/DC converter with its dedicated controller. With this arrangement, if any winding fails, the faulty 3-phase will be removed from DC-bus by converter. Only the healthy 3-phase will keep running, which maintains the power supply to essential on-board devices. The machine is designed with a maximum speed of 14,200rpm. As the M/G system is to be integrated within an aircraft engine gearbox, a high ambient temperature (80-100°C) needs to be considered. Due to the space limit and high-temperature environment, the sensorless control is implemented for this M/G system. Further challenges include very limited space and oil mist environment, which make the M/G system design a very challenging task.

This paper aims to share with the aerospace community the design process of this recently developed M/G system for turboprop mild hybridisation. The following of the paper is organised as follows: Section II introduces electrical machine design; the introduction of power electronics design is in Section III; the introduction of control hardware and control algorithm are in Section IV, Section V introduces the thermal and mechanical design; Section VI presents some experimental result and shows the performance of the developed M/G system, with conclusion in Section VII.

II. Electrical Machine Design

A. Application Requirements

The application of this particular M/G and its integration to an engine PAGB put some specific requirements for such a system including space limitation, power rating, temperature limitation, reliability etc. For the power requirement, it is required that the design target should output at least 20kW electric power during generation mode with a speed range from 12.4krpm to 14.2krpm, giving the minimum torque requirement of 15.4Nm during motoring mode (0-12.4krpm) for green taxiing applications. The torque ripple should be <3% with sinusoidal voltage source and <10% with PWM voltage source. The fault-tolerant design should also be considered with the consideration of two-channel operations. There are also dimension constraints for this M/G such as outer and inner diameter, available length which has been presented in our previous publication [7].

B. Machine Design after Trade-off studies

The machine topology trade-off study has been presented in our previous publication [7], and the output from the trade-off study is a machine with the parameters in Table 1. As can be seen, the machine developed is able to deliver required power (20kW) at both 12.4krpm (24.9kW) and 14.2krpm (26.9kW) with the power converter dc-link at 540VDC. However, the torque ripple is of 6.1% at 12.4krpm. The geometry of the machine can be further optimised to improve the performance parameters such as percentage torque ripple, cogging torque, efficiency, and short circuit current whilst maintaining or increasing the output power from the machine from the trade-off studies.

Table 1
Electrical Parameters of the Machine from Trade-off Studies [7]

PARAMETERS	VALUE	UNIT
Average Winding Temperature	132	℃
Phase Resistance per channel	0.475	Ω
Phase Inductance	440	µH
Output Power at 12.4krpm per channel	24.9	kW
Output Power at 14.2krpm	26.9	kW
Load Torque Ripple at 12.4krpm	**6.1**	%
Load Torque Ripple at 14.2krpm	3.5	%
Efficiency at 12.4krpm	93.2	%
Efficiency at 14.2krpm	93.8	%
Rated Current	23.3	A

Fig. 2(a) shows the radial cross-section of the machine design from the trade-off study. The geometrical input variables that can be further optimized are shown in Fig. 2(b). During the design process, the stator outer diameter, shaft inner diameter and total airgap (including stator and rotor sleeves) are fixed due to the PAGB design. However, other design variables such as tooth width (T_w), slot opening (S_o), slot opening height (S_{oh}), slot depth (S_d), magnet thickness (T_m), central magnet ARC and number of turns per coil (N), can be further optimised to achieve better performance with lower ripples and higher efficiency etc. An in-house Genetic Algorithm (GA) is developed within the University of Nottingham to further optimise the machine design and the details of this process are explained in the next section.

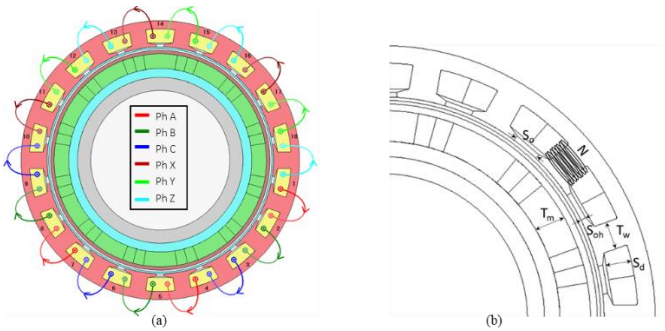

Fig. 2. Existing Machine (a) Radial Cross-section. The phase 1,2 and 3 corresponds to one three-phase unit and phase 4, 5 and 6 is the second three-phase unit (b) Input Variables.

C. Genetic Algorithm Optimisation

1) Genetic Algorithm (GA)

The GA is a method for solving both constrained and unconstrained optimisation problems, based on the natural selection - the process that drives biological evolution. The GA repeatedly modifies a population of individual solutions. At each step, the GA picks individuals randomly from the current population to be parents and uses them to produce the children for the next generation. Over successive generations, the population "evolves" toward an optimal solution [8], [9].

The procedure of GA optimisation algorithm is to find a vector $Y = (y_1, y_2, \ldots, y_n)$, representing a set of design variables, each of them bounded by $y_{im} \leq y_{in} \leq y_{in}$, $i = 1,2,3,\ldots,n$, so that the objective function $F(Y)$ is maximised or minimised, and a set of k constraints $Gj(Y) \leq 0$, $j = 1,2,\ldots,k$, is satisfied [9]. In this paper, GA is implemented which does the following tasks:

- Optimisation Software – the commercial, GA based software package called "Mode-Frontier" by ESTECO is used to maximise and minimise the motor performance parameters.
- Interface – A combined MATLAB-MotorCAD script was developed to carry out the optimisation process. The optimisation software Mode-Frontier was linked with the MATLAB script which calls MotorCAD to solve the machine, based on a GA. In MotorCAD, FE solutions are used to perform a detailed evaluation of every candidate while the machine operating at the base speed and full mechanical load on the shaft.
- Optimisation Approach – the first stage of the optimisation loop is to perform by utilising the design of experiments (DoE) method [10], [11]. Although these are used for many applications, here a DoE based on a random sequence, used to provide an initial population size of 60 individuals with DNA string mutation ratio of 0.05, giving a total of 1200 candidate designs' evaluations.
- The second stage of the optimisation process is to perform exploration of the designs by utilising a multi-objective GA, based on a scheduler designed for Pareto convergence [10]. Subsequently, a refinement is done according to the results obtained in the first stage using

the best solutions as initial population for the second round of optimisation.

2) Geometrical Optimisation

Since the geometrical layout of stator influences the overall performance of the machine [12]–[15], the multi-objective geometrical optimisation was carried out using GA. The main objective of the optimisation is to maximise the output power, phase inductance and efficiency at the same time to minimise load torque ripple, no-load or cogging torque and short circuit current.

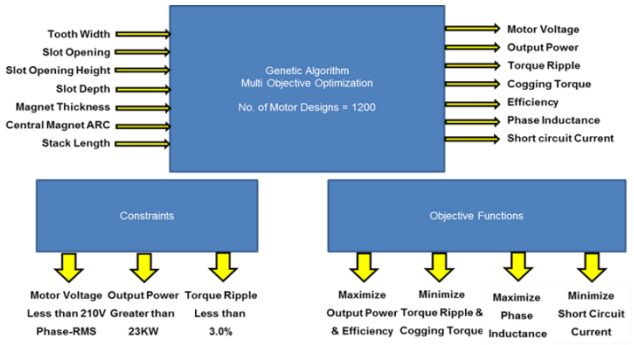

Fig. 3. Block diagram of optimisation process by using genetic algorithm.

Motor terminal voltage, torque ripple, and output power were kept as constraints whereas, the tooth width, slot opening, slot opening height, magnet thickness, central magnet ARC and the number of turns per coil were taken as design input variables as shown in Fig. 3. The constraints include terminal voltage (must be in range between 200V to 210V phase-rms per channel), output power (must be equal or greater than 23kW) and torque ripple (must be less than 3%) that were kept in the loop whereas, the objective functions were defined to maximise the output power, efficiency, d-axis inductance and minimise the torque ripple, cogging torque and short circuit current.

In the design process, the rotor based speed was designed at 12.4krpm as the machine is likely to increase the output power at 14.2krpm, due to an increase in the machine's power factor, in the field weakening region [7], [16]. Also, this is a point (12.4krpm) where maximum saturation of the iron steel occurs (worst case scenario). The current density of the conductor and slot fill factor were also kept constant so that the thermal behaviour of the conductor remains unchanged. This will lead to a fair comparison between the existing and optimised machine design candidate. Since the current density and slot fill factor were kept constant, any change in the slot area in the optimisation process will change the machine's phase current.

3) Optimisation Results and Discussion

In Fig. 4(a)-(e), the values of 1200 candidate designs (1200 candidates corresponds to red and green dots in Fig. 4(a)) as well as the values of objective functions corresponding to the final Pareto-optimal set of designs are shown. All parameters are plotted against the output power as it was the important parameter to be considered for this application. The machine designs that did not meet the specified requirements and constraints were considered as unfeasible designs (i.e., green + sign) and therefore, not considered for the final selection. From the Pareto-optimal set (i.e., red + sign), the percentage torque ripple and peak-to-peak cogging torque are shown in Fig. 4(b) and Fig. 4(c) respectively. In Fig. 4(b), it can be observed that the variation between the torque ripple and the average torque production occurs from values as low as 1.6% to 3.5%, with output power varying from 23 to 26.4kW. Similarly, the variation in cogging torque, given by Fig. 4(c), occurs from values as low as 0.02 to 0.86Nm, with output power varying from 23 to 26.7kW. The variation in short-circuit current form the Pareto-optimal set is varying from the 78 to 114.5A as shown in Fig. 4(d). The horizontal line in Fig. 4(d) represents the constraint of 100A short-circuit current.

On the other hand, as expected, variation in percentage efficiency is very minimal as conductor's current density was kept constant in the optimisation environment, letting no change in the thermal behaviour. The change in percentage efficiency is just 0.43% which can be seen in Fig. 4(e).

4) Challenges & Selection of Machine Design

Machine selection is finalised, based on the challenges and constraints given by the application at the start of initial design phase. The selected machine (black dot) is shown in Fig. 4, the challenges and constraints of which were assigned as:

- The machine must develop the output power of at least 20kW (both channels) at rated conditions.
- Peak Output power of 26kW was required at 14.2krpm rotor speed, giving the overload capacity of 1.30.
- Available DC-link voltage was 540V per channel, providing 220V phase-rms voltage at the motor terminals.
- Rated load torque ripple (fundamental current) must not exceed 3%.
- The peak value of line-to-line Short-circuit current must be minimized and kept under 100A.
- Control platform requires at least 400µH phase inductance per channel to keep the switching current ripple at bay. Therefore, minimizing losses and torque ripple caused by the high frequencies.

As illustrated in Fig. 4(c), the percentage torque ripple of the existing machine reaches the maximum allowable limit whereas, the output power and motor terminal voltage have met the requirements. The comparison of the existing machine and optimized machine is illustrated in TABLE 2.

The criterion for selecting the machine is to reduce the torque ripple and short circuit (SC) current and whilst maintaining the rated torque. In the evolutionary optimisation, we have investigated that the torque ripple increases with the increase in the stator turns due to core saturation. However, the advantages of increasing stator turns are enhancing winding inductance and reducing the SC current by (Isc = flux linkage/d-axis inductance). Therefore, a trade-off between the torque ripple and the SC current was made and the final design was chosen keeping the requirement of SC current to be less than 100A as defined by the application.

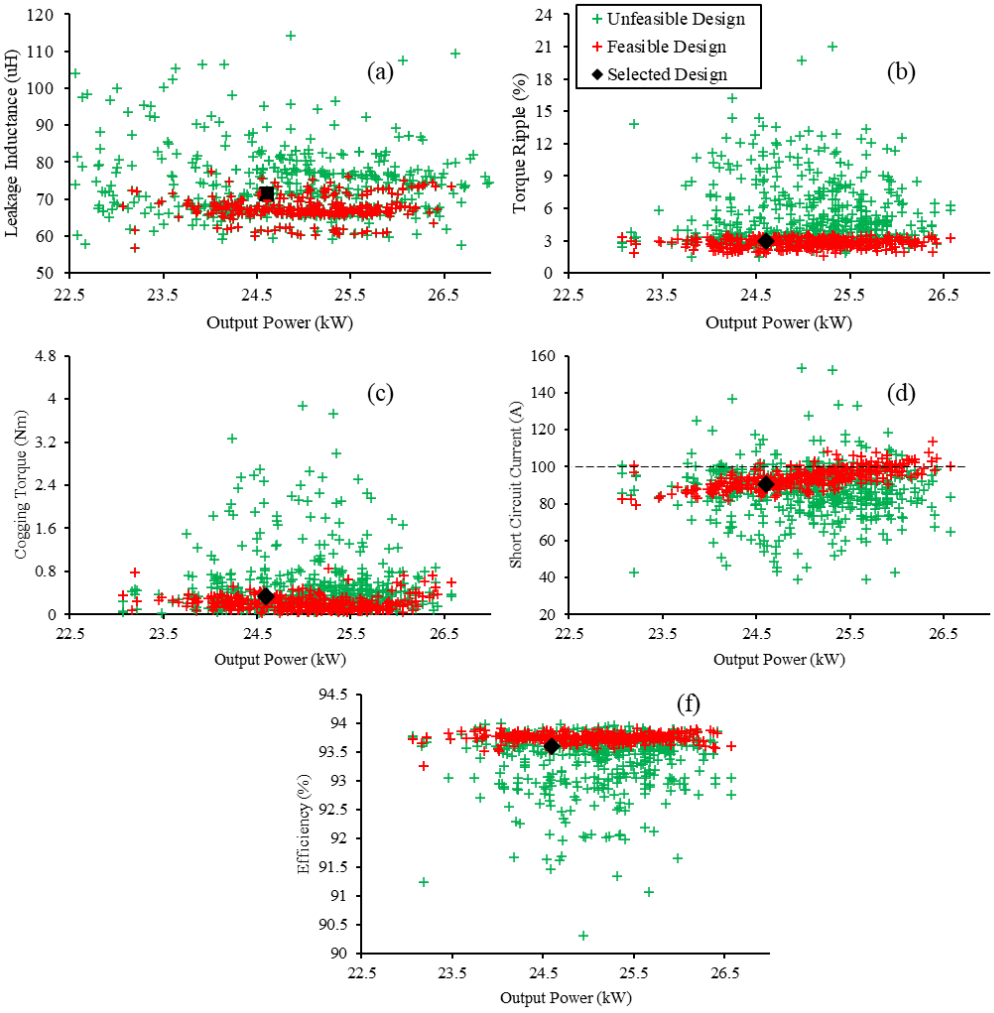

Fig. 4. Optimisation Results (a) Leakage Inductance per Channel (b) Percentage Torque Ripple (c) Peak-to-peak Cogging Torque (d) Peak Line-to-line Short Circuit Current (e) Efficiency

TABLE 2
COMPARISON OF EXISTING AND OPTIMIZED DESIGN

PARAMETERS	Existing Design	Optimised Design	Unit	% Change
Winding Temperature	132	132	C	0
Current Density	24.86	24.86	A/mm^2	0
Phase Inductance per channel	440	450	µH	2.27
Leakage Inductance per channel	71	71.5	µH	0.7
Output Power at 12.4krpm per channel	24.9	24.6	kW	-1.2
Output Power at 14.2krpm per channel	26.9	26.7	kW	-2.5
Load Torque Ripple at 12.4krpm	6.1	3.0	%	-50.8
Load Torque Ripple at 14.2krpm	3.5	0.83	%	-76.2
Efficiency at 12.4krpm	93.2	93.6	%	0.42
Efficiency at 14.2krpm	93.8	94.1	%	0.32
Short Circuit Line Current at 12.4krpm	103.3	95.6	A_{peak}	-7.5
Short Circuit Line Current at 14.2krpm	95.0	90.2	A_{peak}	-5.1

For the final machine design, a significant reduction in percentage torque ripple is observed at the base speed and maximum speed respectively compared to the machine from the preliminary design phase. Moreover, the short-circuit current is reduced by 7.5% and 5.1% at the base speed and maximum speed respectively. The efficiency of the machine is also improved with optimised design.

5) Detailed FE Model of Optimised Machine

The optimised machine is a double layer fractional slot concentrated wound (18s/12p) with a winding factor of 0.87, the winding layout of which is illustrated in Fig. 2(a). The machine includes two channels of 3-phases where each channel provides half the rated power, fed by a separate converter via common DC-link. The machine offers electrical, physical, and magnetic isolation between the two channels. The cooling ducts also ensures that the coils of different lanes are isolated from physical and electrical point of view. The FE model (Fig. 5) was built using MagNet software by Infolytica to validate the output torque and torque ripple at both 12.4 and 14.2krpm with PWM waveforms injected from control simulations. The radial cross section and flux density plot of optimised machine are shown in Fig. 5, where top half represents the FE model and bottom

half represents the flux distribution at 12.4krpm. The machine is operating at flux density of 1.53, 1.56 and 1.0 Tesla in stator tooth, stator and rotor back iron respectively, which is near the knee point in material's B-H characteristics.

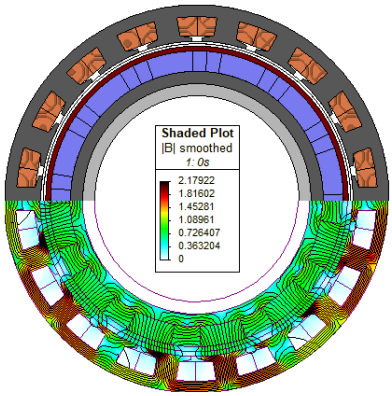

Fig. 5. FE Model and flux distribution of optimised machine

Fig. 6(b) shows the output torque of the machine when PWM currents were injected in both the channels (i.e., in all 6 phases) to investigate the effect of high frequencies on the torque ripple since one of the application requirements was to limit the percentage torque ripple less than 10% when both channels are under healthy condition. As can be seen from Fig. 4(b) that the torque ripple is increased from 3.0% to 7.1% at 12.4krpm with respect to the machine when supplied with sinusoidal currents only. On the other hand, the torque ripple is increased from 0.83% to 6.1% at 14.2krpm. This is an order of magnitude less than the torque ripple allowed from application point of view which is unlikely to cause any disturbance to the mechanical load on the shaft. The reason of having lower torque ripple at higher speed is the field weakening control of the machine beyond the speed of 12.4krpm. Once the machine goes into the field weakening mode iron saturation level shift towards linear region of its B-H characteristics thereby inducing lower saturation harmonics into the machine at 14.2krpm.

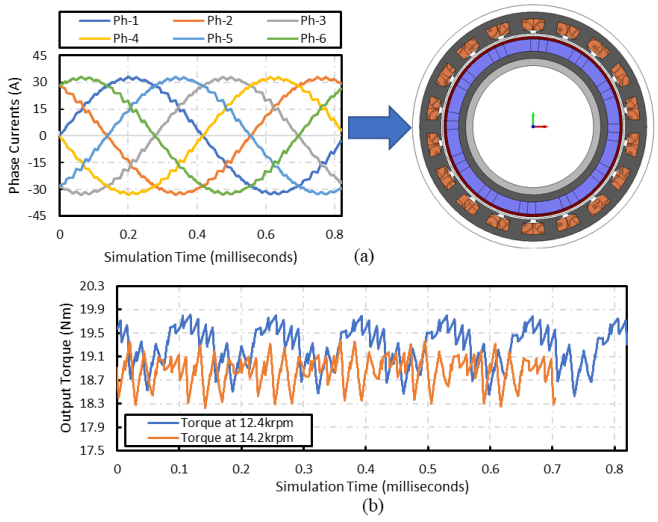

Fig. 6. FEA Model and Results (a) PWM Phase currents from control simulations (b) Torque when machine is supplied by PWM currents at full-load

III. Power Electronic Converter Design

A. Converter structure and design challenge

The progress in the development of semiconductor materials, e.g., Silicon Carbide (SiC) and Gallium Nitride (GaN), is acting as a key factor in improving the power density of converters. This is mainly because such technologies are capable of high dA/dt and dv/dt, thus allowing higher switching frequencies which consequently reduces the size of the input side DC-link capacitor and output side filter inductance. When compared with Silicon (Si) technologies, improvements in volumetric power density up to a factor of 10 has recently been seen with SiC [17], [18]. Various SiC based power converters with power densities ranging from 2kW/L up to 25kW/L have been reported in [17], [19]–[21]. Not only that but even a 50kW/L cubic-shaped SiC based three-phase two-level (2L) inverter system has been also been introduced [22] which indicates the feasibility of very high power density converters. However, in case when the demanded shape or envelope of the converter system is other than cubical, realizing a compact converter becomes extremely challenging as not only the size but the position of electronic components including DC-link capacitors, gate driver ICs, isolated DC/DC supplies and DSP (Digital Signal Processor) also becomes a constraint.

The selection of the semiconductor technology i.e., SiC or GaN is usually based on the required application. For the application of motor drive control, a very fast switching period is not preferable as the studied M/G drive system is using a sensorless control and the DSP may not be able to perform complex calculations. A practical range of switching frequency for such motor-drive application is 30-50 kHz [22]. The advantages of GaN devices becomes dominant over those offered by SiCs when the switching frequency is over 100kHz[23], therefore, SiC devices are preferable for selected for the range of 30-50kHz switching frequency.

It must be noted that in the targeted application, the small volume and the irregular shape are the key limitations. Therefore, the main priority of selecting converter topology is with lower volume. Although, considerable improvements in switching losses are possible using a three-level (3L) converter [24], [25], this comes at the cost of increased number of switching devices. This, in return, leads to increased size and volume of the power converter. In this regard, a SiC based 2L converter was designed and populated on the given envelope.

The actual converter boards assembly is shown in the Fig. 7, and it includes 4 boards in total (i.e., connector board, control board, driver board and power board). The control board is responsible for running machine control algorithm and communication with PC. Driver board converts DSP control signals to isolated SiC drive signals with dead band protection. The power board has two customised SiC modules from Semikron. Each module has one 3-phase full-bridge SiC circuit with maximum DC voltage of 1200V and maximum peak current of 60A under serious condition. In our application, the requirement of converter is shown in TABLE 3. As can be seen from it, the DC link voltage is 540V and the maximum peak current is 30A, which has much safe margin to the device

absolute maximum ratings.

TABLE 3
REQUIREMENTS OF POWER CONVERTER

Parameter	Value
Input DC voltage	540V
Maximum output phase AC voltage magnitude with SVPWM	311V
Maximum output phase AC current magnitude	30A
Maximum output active power requirement for whole converter	20kW

In Fig. 7, two 10uF capacitors and many 0.1uF ceramic capacitors are soldered on the 540V DC-link. Due to the irregular shape of boards, the 0.1uF small size capacitors are stacked in the empty area of power board as much as possible to reduce ripple on 540V DC-link. There are 6 current sensors on the power board as well to measure six phase currents.

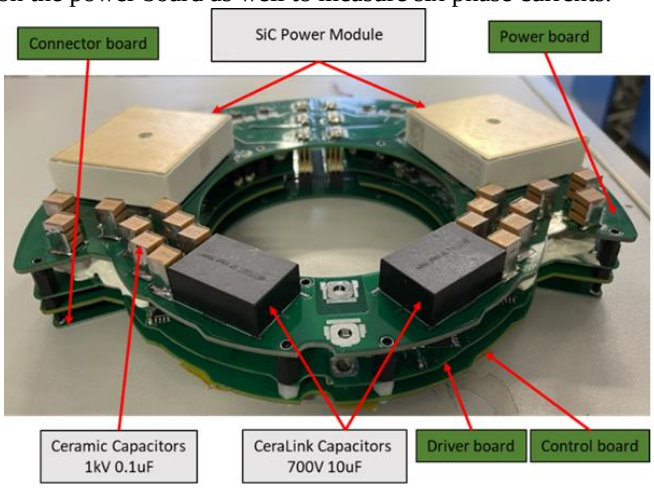

Fig. 7. Real converter boards assembly

B. Experimental validation of dual three-phase converter with RL load

In order to validate the prototype of the power converter, an experimental setup has been built the photo of which is shown in Fig. 8. The dual 3-phase converter has been integrated into the customized lid and heatsink. A water chiller pumps coolant through the heatsink to take away the heat generated by SiC module. Two 270V DC power supplies (Delta-Elektronika SM500-CP90 with 500V and 90A) are cascaded to build a 540V DC bus for the converter. This voltage level buses are now common in more electric aircraft as they offer several advantages specifically increased gravimetric power density and capacity when compared with traditional voltage levels [26]. A 6-phase RL (resistor-inductor) load with parameters listed in TABLE 4 is connected to converter terminals. It consists of 2 independent star-connected 3-phase RL (Resistor and Inductor) loads. The inductors can smooth the phase currents. In addition, another small power supply offers 28V DC voltage to the converter and an oscilloscope is used to record waveform.

TABLE 4
CONVERTER RL LOAD PARAMETERS AND TEST RESULT

Parameter	Value
Resistance per phase for RL load	9.9Ω
Inductance per phase for RL load	1mH
Experimental phase current peak	26.0A
Power output for dual 3-phase	20.08kW
Power density including lid and heatsink	11.8kW/L 9.2kW/kg

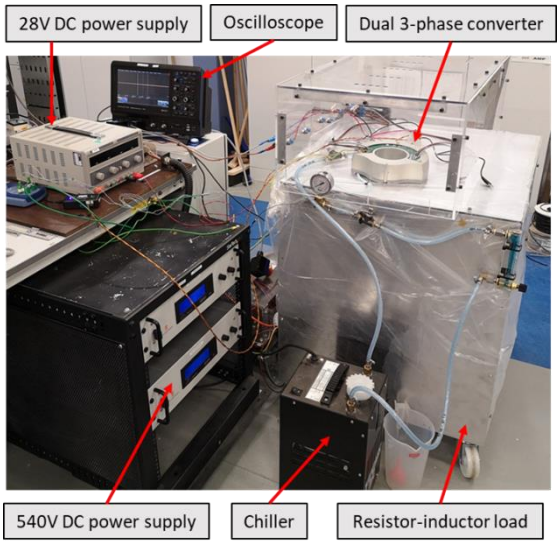

Fig. 8. Experimental setup of a SiC based dual 3-phase converter.

The recorded experimental result, given in Fig. 9, shows the waveforms of phase currents and line-line voltages for one 3-phase channel. The control algorithm is current close loop with SVPWM. As can be seen from Fig. 9, the phase current peak is controlled to 26A. Combining the peak current with resistance of RL load in TABLE 4, the output active power can be calculated with equation (1) and its value is 20.08kW, which has reached the requirement of machine (20kW). The line-line voltage waveform in Fig. 9 are clean from any un-wanted pulses due to accidental turn-on of devices. Based on the converter case volume calculated from CAD design file, the power density in column of whole converter including lid and heatsink is 11.8kW/L. The weight of the whole converter is also measured to calculate the power density in weight, which is 9.2kW/kg. Above all, these key performance indicators (also listed in TABLE 4) prove this converter has reached the design requirement with highly integrated assembly and high power density.

$$P_{6phase} = 6I_{rms}^2 R_{load} = 20.08\text{kW} \quad (1)$$

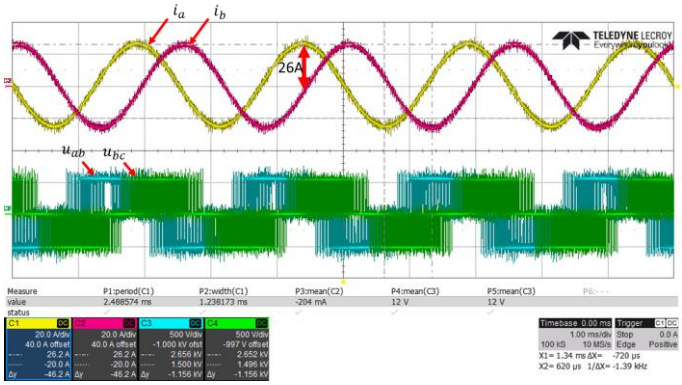

Fig. 9. Experimental waveform of phase currents and line-line voltages when converter output power is 20kW

The experimental efficiency and loss of the converter under different power output are measured by power analyser and shown in Fig. 10. The converter efficiency will increase with power increasing and reaches to 97.9% when DC power is over 18kW. The power loss of converter at 18kW is below 400W. This high efficiency is contributed by the application of high bandwidth power module.

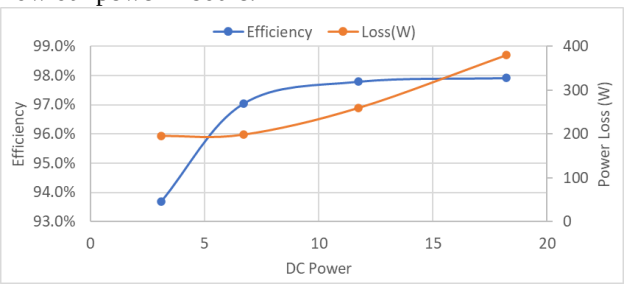

Fig. 10. Experimental result of efficiency and power loss for one three-phase converter.

Above all, this chapter discuss the design and test of power electronics converter. Due to the limited and irregular space for converter, high bandwidth SiC is selected considering the space limit and power rating. The converter is formed by 4 PCB boards and 1 housing. These 4 boards are specially designed considering the balance between good performance and small volume. The housing envelope is designed depending on the spare room inside turboprop engine. The heatsink is also integrated into the housing to reduce volume of the converter furthermore. Finally, all components of converter are assembled together and reach required demand at real test on RL load.

IV. Controller Design

A. Controller hardware design

The controller plays the role of communication, machine control and fault protection for the ACHIEVE system. Considering the request of redundancy, two DSPs (Digital Signal Processor) with one for each three-phase channel separately are used. This design makes sure in the case of one microprocessor fails, there is still another one standby to take over the system control. It can also be seen that the communication interfaces include CAN, USB and JTAG as shown in Fig. 11. This CAN communication allows the host PC sending command to microcontroller and also receiving data from the controller to monitor system status during the system operation process. The JTAG and USB connectors are used for debugging only.

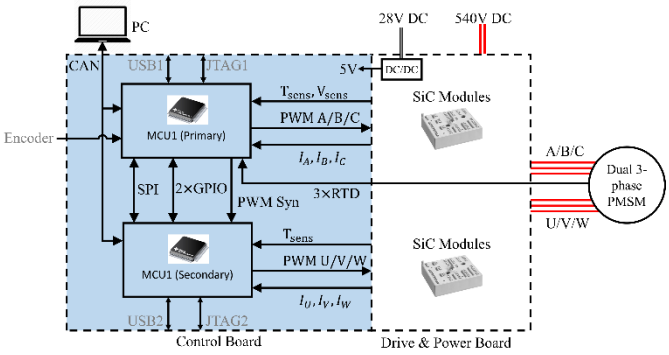

Fig. 11. Control board signal diagram

B. Operation mode

There are two operation modes of M/G system, one is the green-taxiing motoring mode, which requires the M/G to drive propeller from zero speed to a rated speed of 12.4krpm. The other is the generating mode, which requires that machine generates at least 20kW electric power within the speed range of 12.4krpm to 14.2krpm.

In the motoring mode, the machine acceleration procedure is shown in Fig. 12. Due to the lack of rotor position sensor, sensorless control is applied during the whole procedure. There are two categories of sensorless control commonly used in low speeds, i.e. open-loop sensorless (V-F [27] or I-F control [28]–[30]) and close-loop sensorless such as high frequency injection [29], [30]. In our application, the I-F open-loop sensorless control [28] is adopted from zero speed to 300rpm due to its advantages of easy implementation and relatively high robustness. Furthermore, this low-speed range only occupies very small percentage of whole operation time thus the I-F open-loop is a reasonable choice. Once the machine speed is driven to 300rpm, a switch algorithm is applied to make sure the machine switch from I-F control to close-loop sensorless control smoothly. The close-loop sensorless used in high speed range is Model Reference Adaptive System (MRAS) based sensorless control due to its great advantages like simple structure and robustness [31]. Comparing with I-F open-loop control, MRAS sensorless is more suitable for high-speed applications as it is based on back-EMF to estimate rotor position.

The MRAS sensorless control is applied in the generating mode as well. In generating mode, the machine is driven by the turboprop engine with its speed varying between rated speed and maximum speed shown in Fig. 13. The machine absorbs mechanical power from the engine shaft and generates electric power to DC-link. The machine should respond rapidly to the power requirement and keep output DC-link voltage constant with a time-varying shaft speed.

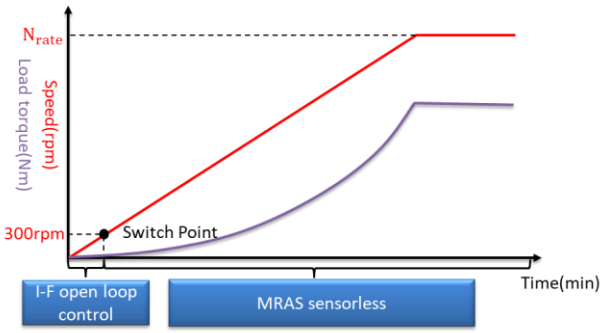

Fig. 12. Machine acceleration procedure at green-taxiing motoring mode

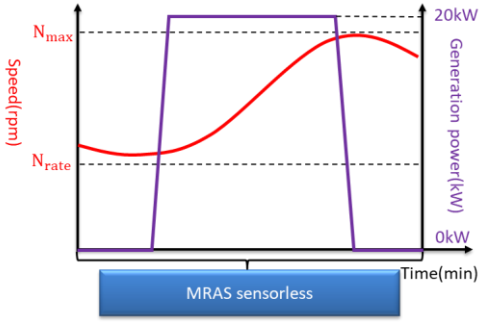

Fig. 13. Generating mode machine operation diagram

C. Control algorithm

1) Green-taxiing motoring mode

As mentioned before, during the motoring mode, the machine control will switch from I-F control to MRAS sensorless control at 300rpm. The reason of not using MRAS sensorless directly is due to its poor performance at extreme low speed. Fig. 14 shows the change of speed reference (ω_m^*) and q-axis current reference (i_q^*) during the switching period. There are 4 stages in total during motoring operation.

In stage 1, ω_m^* is set to 0 and i_q^* will initially build up linearly from zero. During this stage, the machine rotor will clamp to a position where rotor flux vector is aligned with stator flux vector. The ramping change of i_q^* smooth the clamping process to avoid shock to the bearing. To deal with different friction torque, the slope and final value of i_q^* can be adjusted to provide enough electromagnetic torque and ensure safe clamp.

In stage 2, i_q^* will keep constant with ω_m^* increased gradually. The rotor position ($\tilde{\theta}_e$) comes from the integration of ω_m^*. Within this stage, the rotor speed will follow the reference (ω_m^*) with open-loop IF control. The slope of ω_m^* can be adjusted based on the different friction torque and load inertia.

When the ω_m^* reaches its plateau at 300rpm, the system will enter stage 3 where ω_m^* will keep constant and i_q^* is set to be reduced gradually. While i_q^* is reducing, MRAS sensorless algorithm is running in background to calculate estimated rotor position ($\hat{\theta}_e$). A position error ($\tilde{\theta}_e - \hat{\theta}_e$) will be used as criteria of switching from I-F open loop control to MRAS sensorless control. The switching happens when the position error small enough ($< 5°$ in our test) to ensure the stability.

In stage 4, switching finishes and the $\hat{\theta}_e$ from MRAS sensorless algorithm will be used in voltage and current Clarke-Park transform, and the estimated speed ($\hat{\omega}_m$) from MRAS sensorless is used as speed feedback for speed PI controller. i_q^* will be adjusted by speed PI controller instead of following a programmed curve. Till now, the low-speed start-up procedure has finished, and MRAS sensorless estimation algorithm will used to control the machine from this stage.

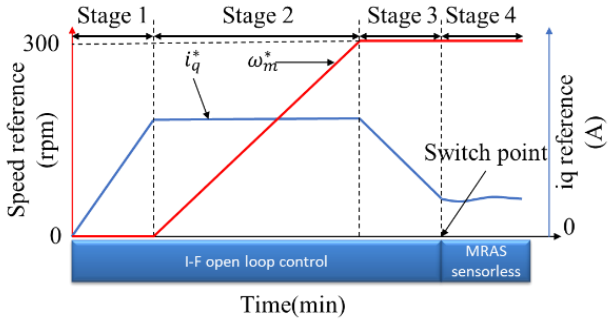

Fig. 14. Speed and q-axis current reference under I-F open-loop control

The control algorithm running at green-taxiing motoring mode is shown in Fig. 15. The two overlapped yellow areas represent the algorithm running in two DSPs. Each DSP control one three-phase converter. There are two switches (red circles) in Fig. 15 representing the switching procedure discussed above. I-F open-loop control is running with switches at position 1 and MRAS sensorless control is running at switch position 2. After switching from position 1 to 2, the MRAS sensorless algorithm (blue area in Fig. 15) estimates rotor position and speed in real-time, which are used by speed and current closed-loop control. The detail of MRAS sensorless control will be explained in the following subsection.

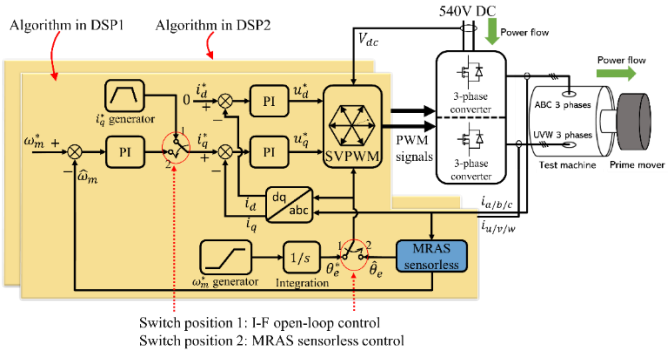

Fig. 15. Control diagram for green-taxiing motoring mode

2) Sensorless control algorithm

The sensorless control is one of the most challenging issues of this drive system. Although the MRAS has been developed for more than two decades[32]–[34], this high speed application background requires careful design of MRAS structure to avoid instability and low accuracy. The control diagram of MRAS sensorless estimation is shown in Fig. 16. The 'Adaptive Model' can be regarded as a digital twin of the actual machine, fed with the actual machine's input voltages, and expected to get the same speed and currents information of the actual

machine. The 'Control Rule' is specifically designed to ensure the algorithm stability is guaranteed by Popov Super Stability Theorem [31]. When $\hat{\imath}_d = i_d$ and $\hat{\imath}_q = i_q$, the error of control rule will be zero, and the adaptive model running in the microcontroller can be regarded as identical of the actual machine. In that case, the estimated speed and position from adaptive model can represent the actual machine speed and position.

The electrical fundamental frequency (f_e) is 1.24kHz when the machine speed is 12.4krpm. Although the PWM frequency (f_{pwm}) can reach to 40kHz benefiting from the SiC modules, the ratio of f_{pwm} to f_e is still very small, which can deteriorate the control accuracy and stability [35]. Therefore, accurate controller discretization and delay compensation are critical in this application. A detailed MARS sensorless controller design for such a system will be detailed in another paper which is under review.

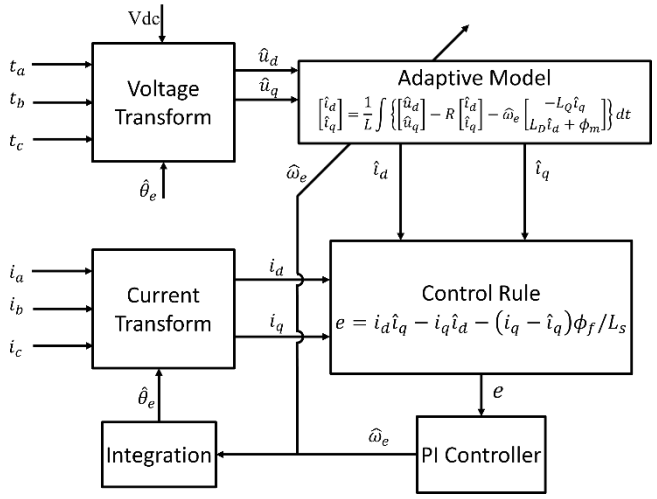

Fig. 16. Control diagram of MRAS sensorless estimation

3) Generating mode

In the generating mode, the control diagram is shown in Fig. 17. The current control loop and MRAS sensorless algorithm is the same with motoring mode, but using voltage droop control as outer control loop [36]. Same with motoring mode, the control frequency is same with converter PWM frequency (40kHz).

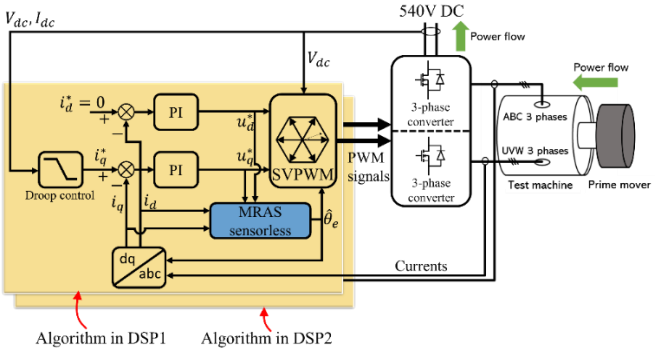

Fig. 17. Control diagram for generating mode.

V. Thermal and Mechanical Design

A. Thermal and mechanical design ideas

A thermal management of the M/G was conducted to identify an efficient and reliable cooling solution for both machine and power electronics. Based on power losses previously estimated, some thermal analyses were conducted about the temperature field. The distribution of losses and the dependency of some of them upon the temperature, suggested that a very effective cooling was required. In order to develop this, a range of cooling options, all based on liquid cooling were considered.

The thermal design was carried out considering the following design criteria:

- **Effectiveness**: the cooling system must guarantee an effective dissipation of power losses from the machine to maintain temperatures within acceptable limits. For the most critical parts of the machine, such as the magnets and the stator windings, the maximum allowable temperatures of 180 °C and 250 °C respectively, have been assumed. Electronics baseplate must be kept below 70 °C due to limited operating temperature of DC/DC components.
- **Size**: given the limitations in terms of space, for this application, the cooling system must be compact in order not to exceed size limits.

The availability of liquid mediums on board such as oil and fuel allow both direct and indirect liquid cooling options to be considered i.e. Jacket cooling and Wet Stator, the coolant can also be shared between the machine and the power electronics. Liquid cooling can furthermore lead to more effective and compact designs [37].

The main challenge of cooling the integrated machine/electronics design comes from the fact that the operating environment has a temperature well above that permitted by the electronics components which is 70°C. The engine ambient operating temperature is 80°C-100°C. As all the electronics needs to be attached to the machine due to space constraints. it was decided to implement an integrated cooling configuration as shown in Fig. 18. The coolant (Turbo Oil 2389) enters the heatsink where the heat from the power modules is dissipated; following that the fuel floods the machine. Due to the fact that windage loss is directly proportional to the fluid viscosity and to the cube of the rotational speed, significant viscous heat will be generated in the machine air-gap. A wet stator solution was implemented in the developed M/G. This implies that an intensive direct cooling of the stator whilst the rotor is physically separated from the stator region by inserting stator sleeve through the airgap.

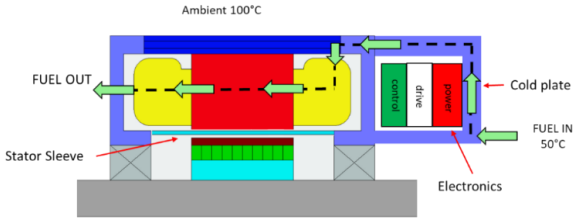

Fig. 18. Schematic Cooling Configuration

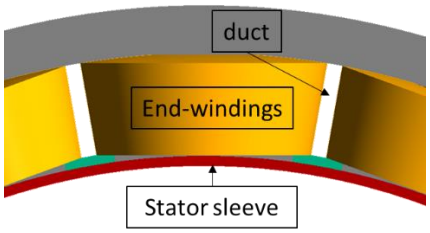

Fig. 19. Stator Axial Ducts

Once the coolant leaves the cold plate it enters the stator chamber through an axial inlet and then it flows through the stator in 1.5 mm wide axial ducts created between the concentrated windings inside the slot as shown in Fig. 19 before leaving the machine. A nominal flow rate of 6 lt/min was set for this design.

B. *Converter thermal analysis*

The cold plate for the electronics consists of a finned surface with fins height of 6 mm with a thickness/spacing of 1 mm; the fin length is equal to the power modules length (59 mm). Power modules are assumed to be generating 200W each when delivering a rated power of 10kW. A customized design as shown in Fig. 20 was produced in order to be able to fit the system within the boundaries of the envelope. The volume of the whole cooling system including cold plate and the fluids is 0.341L.

In order to minimize the overall pressure drop, the finned surfaces were only located just under the power modules; furthermore the cold plate inner flow path was accurately designed to achieve gradual velocity changes in the flow. Indeed, some numerical analyses (CFD) were carried out to investigate the fluid flow inside the cold plate. As it can be seen in Fig. 20 a quite uniform flow distribution is obtained with a reasonably low pressure drop of maximum 0.2 bar.

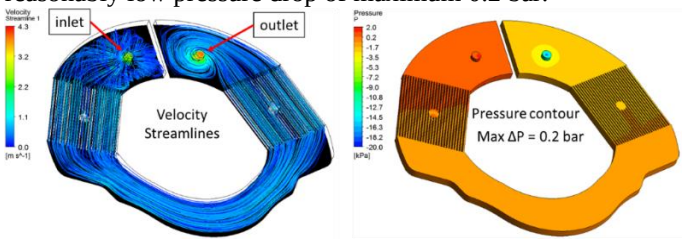

Fig. 20. CFD fluid analysis of cold plate

The fins design was carried out analytically, fin effectiveness and efficiency were then optimized in order to maximize their cooling effect. Following that, a numerical approach was used to confirm the analytical prediction and to estimate the temperature distribution on the conductive plate as shown in Fig. 21; it can be seen that the plate temperature stays within the maximum temperature limit allowed of 70°C, also the average plate temperature agrees well with the one predicted analytically ($T_{av(analytical)}$ =61°C).

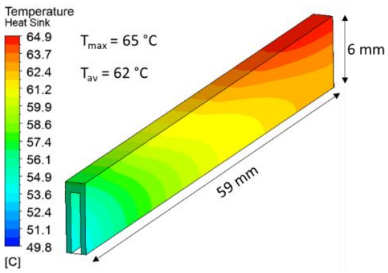

Fig. 21. Temperature distribution of baseplate

C. *Machine thermal analysis*

A conjugate heat transfer analysis, including fluid flow and heat transfer, was also carried out to analyse the thermal behaviour of the machine. Given the axisymmetric nature of the design, only 1/6th of the whole domain was considered, that is to reduce the computational cost of the simulation.

A steady-steady condition analysis only was considered and at the highest operating point, where the highest losses take place and the machine is supposed to operate for most of its time. The surrounding environment was assumed to be at 100°C as mentioned above due the fact that the system is located in such harsh environment like the gearbox.

Fig. 22 shows the temperature distribution estimated in both stator and rotor region. For a better clarity, the stator temperature field only is shown as well. As it can be seen the coolant is capable of maintaining the windings well below the maximum allowable temperature which is 250°C and the fuel temperature rise between machine inlet and outlet is only 11°C. The hotspot in the stator was observed in the middle of the windings as it could be expected, whilst in the rotational region the highest temperature was observed in the bearing(147°C) which has a maximum temperature allowed of 160°C; that is mainly due to the lack of active cooling which can dissipate the high friction loss.

The fluid flow inside the machine was also analysed, this allowed to predict the pressure drop across the machine which is just 0.02 bar (20 kPa).

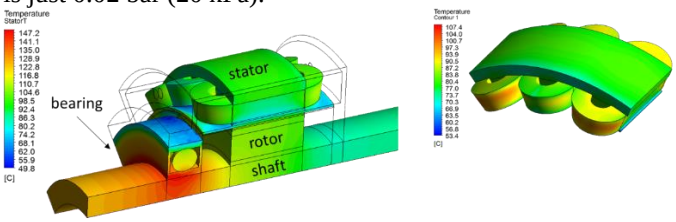

Fig. 22. Machine temperature profile

D. *Whole system structure and cooling plan*

Analytical and numerical analyses have shown that despite operating in a high temperature environment, the integrated system consisting of the machine and power electronics can run within safe temperature levels by adopting the integrated liquid cooling configuration described. The total pressure drop achieved, only 0.22 bar, allows operating the system at low pressure, therefore thinner and lighter structures can be used, and this represent an important benefit for an aerospace application.

Fig. 23 shows the overall assembled system consisting of both machine and converter. The two components are electrically and mechanically coupled. As described above they also share the same coolant. This is supplied externally, and it is first connected to the converter cold plate and the coolant temperature will become higher by absorbing SiC module loss. Then the coolant will go to machine winding and its temperature will increase more by absorbing the machine loss. Finally, the high temperature coolant will flow back to chiller from coolant outlet shown in Fig. 23.

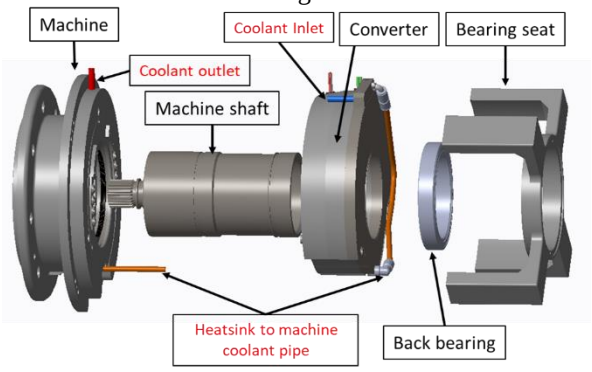

Fig. 23. Exploded view of whole system.

VI. Experimental Result

A. Test rig introduction

To validate the dual three-phase machine drive system with its cooling system, a test rig with a diagram on Fig. 24 and real pictures on Fig. 25 is built. The prime mover system can operate in the torque control mode and the speed control mode, which can simulate the aircraft green-taxiing motoring and generating mode respectively. The control panel of the prime mover is placed in the control room whilst the induction machine and drive are in the high-speed test room. The dual three-phase converter, machine and cooling system are placed in the high-speed test room as well. As can be seen in Fig. 25, the converter is separated with the machine temporarily for the convenience of debugging. They will be fully integrated for the final test in PAGB.

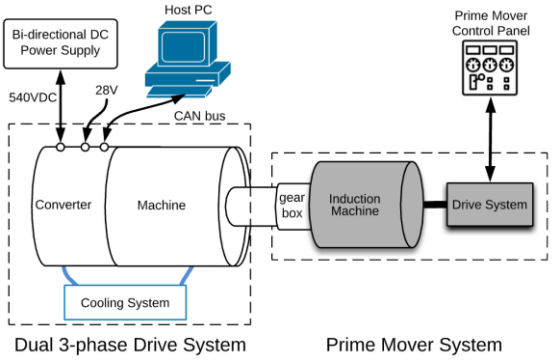

Fig. 24. Diagram of dual three-phase drive system test rig

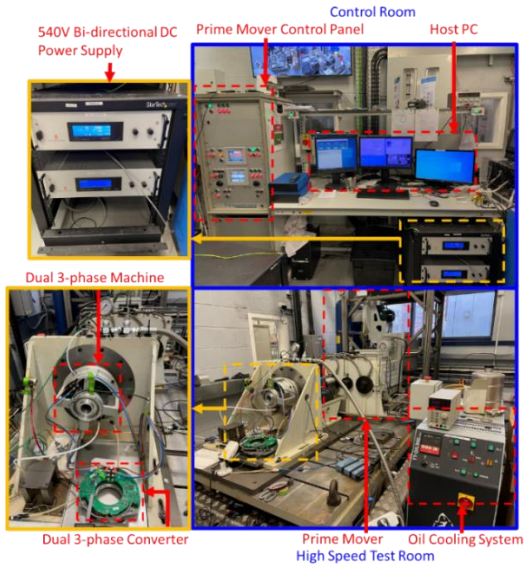

Fig. 25. Dual three-phase drive system test rig setup

B. Green taxiing motoring test

In green taxiing motoring mode, the dual three-phase machine should drive the propeller from stop to rated speed. The test below simulates this procedure by disconnecting the induction motor with its drive and regarding its rotor as the propeller. Fig. 26 shows the experimental result of I-F open-loop start-up and the switching to MRAS sensorless. The speed and currents waveform in Fig. 26(a) and (b) match with the expected waveform in Fig. 14. The switching point represents the switching moment from the I-F open-loop control to the MRAS sensorless control. In Fig. 26(c), the angle difference between the I-F control and the MRAS converges to zero with i_q reducing. Once this difference is small enough ($< 5°$ for example), the switching will be triggered. As can be seen from Fig. 26, the switching procedure is smooth.

Fig. 27 shows the acceleration under the MRAS sensorless control from 300rpm to the maximum speed (14200rpm). Due to the prime mover inertia being much smaller than a real propeller, the speed accelerates very fast (under 60 seconds) with a q-axis current below 5A. It can be seen from Fig. 27(a) that the speed reaches 14200rpm smoothly without a large overshot, and the currents are stable during the whole procedure, which represents the good acceleration performance.

TABLE 5
TEST RESULT UNDER GENERATING MODE WITH DIFFERENT Q-AXIS CURRENTS

Speed (krpm)	i_q(A)	Generating power(kW)	Mean torque(Nm)	Total loss(W)	Total efficiency
12.4	0	-0.28	0.20	535	
12.4	-10	6.37	5.29	499	92.73%
12.4	-20	12.54	10.35	900	93.31%
12.4	-30	18.33	15.21	1421	92.81%
14.2	0	-0.26	0.18	523	
14.2	-10	7.30	5.32	611	92.28%
14.2	-20	14.50	10.38	935	93.94%
14.2	-30	20.94	15.19	1648	92.70%

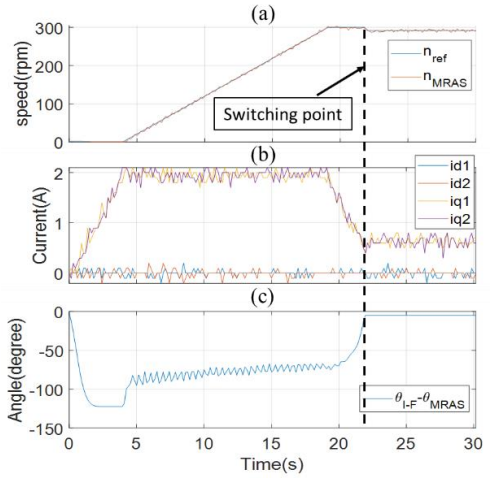

Fig. 26. Speed and current waveform for the I-F open loop start-up from 0 to 300rpm.

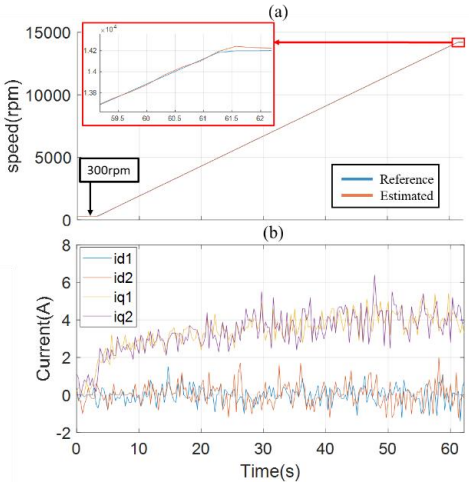

Fig. 27. Speed and current waveform for the MRAS sensorless control acceleration. (a) speed acceleration from 300rpm to 14200rpm. (b) d/q-axis current during acceleration.

C. Generating mode test

In generating mode, the prime mover is running under speed-controlled mode with speeds between 12400rpm and 14200rpm. The generating power of the dual three-phase machine drive system is controlled by adjusting the q-axis current (i_q) of the machine. A serial test has been done under 12.4krpm and 14.2krpm with different i_q, and the result is shown in TABLE 5. The prime mover holds shaft speed constant at the selected speed. Mean torque is measured by a torque sensor in prime mover system, and generating power is got from 540V DC power supply. The total loss is the difference between the mechanical power to dual three-phase machine and the electrical power absorbed by DC power supply, which includes bearing friction loss, machine copper loss, iron loss and converter loss. Although the total loss increases significantly with higher generating power, the total efficiency is almost the same. The total efficiency is 92.7% when the speed is 14.2krpm and the generating power is 20.94kW. Under this situation for several minutes, the SiC temperature is stable at 90°C, which is still below the temperature limit of this module (125°C).

Fig. 28 shows the experimental result under 12400rpm and $i_q = -30\text{A}$. The estimated speed can track the real speed although there is some noise on it. The d/q-axis currents can hold constant at their command values. The duty cycle is a standard SVPWM waveform with fundamental frequency and its third harmonics. Fig. 29 shows the result under 14200rpm and $i_q = -30\text{A}$. Similar to Fig. 28, the control algorithm can track speed and currents command very well.

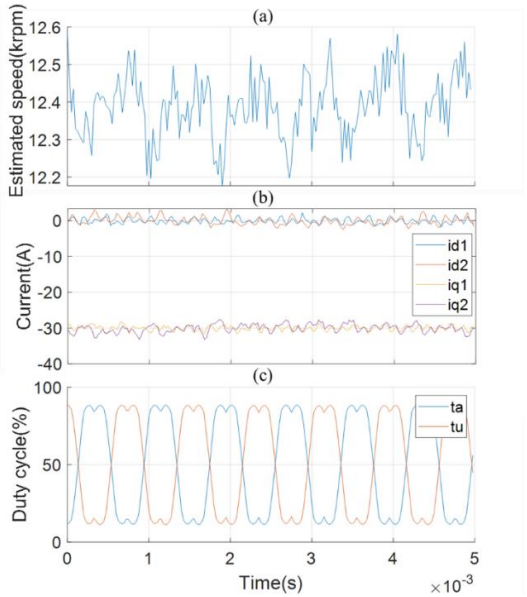

Fig. 28. Estimated speed, duty cycle and d/q-axis currents at speed=12400rpm, iq=-30A, sample frequency=40kHz. (a) estimated speed, (b) d/q-axis currents, (c) duty cycle of A and U phase

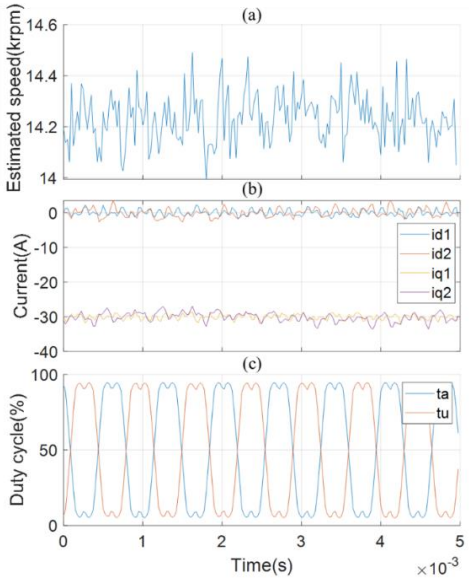

Fig. 29. Estimated speed, duty cycle and d/q-axis currents at speed=14200rpm, iq=-30A, sample frequency=40kHz. (a)

estimated speed, (b) d/q-axis currents, (c) duty cycle of A and U phase

VII. Conclusion

This paper presents a high-power-density integrated electric drives for mild hybridization of turboprop engines. The drive system includes a dual three-phase PMSM, a SiC converter and a corresponding cooling system. Each part is designed specifically to allow the drive to operate under limited space and harsh engine environment (high temperature with oil mist).

For the machine design, it must be divided into two three-phase channels in order to meet the fault tolerance and reliability requirements. Slots/poles combination and winding configuration are determined to ensure required power generation within a limited space. Stator geometry is optimized by a genetic algorithm to improve performance furthermore.

The challenge of converter design comes from the irregular shape and high power density. The high bandwidth device SiC module is applied to increase power density. Due to the high integration demand, the controller board is customized and placed inside the converter. In order to reduce the EMI of the converter, the gate driver is tested and optimized to reduce ringing. Finally, a high power density converter of 11.8kW/L is achieved.

The main challenge of control is whole operating range sensorless control. Any position sensor is impossible to install due to the limited space and high temperature inside the engine. Different Sensorless algorithms are adopted for low and high speed and switching rule makes sure smooth transitions between the two algorithms. In addition, dual DSPs structure is used to improve reliability and firmware upgrade through CAN bus is developed for the convenience of further maintenance.

An efficient and reliable cooling solution is required for both converter and machine. A fuel cooling system is developed to allow the whole system to operate at rated power within up to 100°C engine ambient. The converter cold plate is designed to become part of the converter case to reduce size. The fuel goes to the cold plate first and then to the stator axial ducts between windings. A 6 lite/min flow rate is validated by numerical analyses for full-power operation.

Finally, a prototype of the drive system is manufactured and tested on a test rig to simulate the engine condition. Both green taxiing motoring mode and generating mode are tested under maximum speed (14200rpm) and rated power (20kW). The sensorless algorithm works well in all situations. The cooling system provides enough heat dissipation ability at rated power for all parts.

References

[1] W. Cao, B. C. Mecrow, G. J. Atkinson, J. W. Bennett, and D. J. Atkinson, "Overview of electric motor technologies used for more electric aircraft (MEA)," IEEE Trans. Ind. Electron., vol. 59, no. 9, pp. 3523–3531, 2012, doi: 10.1109/TIE.2011.2165453.

[2] J. A. Rosero, J. A. Ortega, E. Aldabas, and L. Romeral, "Moving towards a more electric aircraft," IEEE Aerosp. Electron. Syst. Mag., vol. 22, no. 3, pp. 3–9, 2007, doi: 10.1109/MAES.2007.340500.

[3] V. Madonna, P. Giangrande, and M. Galea, "Electrical Power Generation in Aircraft: Review, Challenges, and Opportunities," IEEE Trans. Transp. Electrif., vol. 4, no. 3, pp. 646–659, 2018, doi: 10.1109/TTE.2018.2834142.

[4] S. Bozhko, S. S. Yeoh, F. Gao, and C. Hill, "Aircraft starter-generator system based on permanent-magnet machine fed by active front-end rectifier," IECON Proc. (Industrial Electron. Conf., pp. 2958–2964, 2014, doi: 10.1109/IECON.2014.7048930.

[5] S. Gunter et al., "Load Control for the DC Electrical Power Distribution System of the More Electric Aircraft," IEEE Trans. Power Electron., vol. 34, no. 4, pp. 3937–3947, Apr. 2019, doi: 10.1109/TPEL.2018.2856534.

[6] A. Barzkar and M. Ghassemi, "Electric power systems in more and all electric aircraft: A review," IEEE Access, vol. 8, pp. 169314–169332, 2020, doi: 10.1109/ACCESS.2020.3024168.

[7] M. R. Khowja, G. Vakil, C. Gerada, T. Yang, S. Bozhko, and P. Wheeler, "Trade-off Study of a High Power Density Starter-Generator for Turboprop Aircraft System," IECON Proc. (Industrial Electron. Conf., vol. 2019-Octob, pp. 1435–1440, 2019, doi: 10.1109/IECON.2019.8926961.

[8] S. L. Ho, N. Chen, and W. N. Fu, "An optimal design method for the minimization of cogging torques of a permanent magnet motor using FEM and genetic algorithm," in IEEE Transactions on Applied Superconductivity, 2010, vol. 20, no. 3, pp. 861–864, doi: 10.1109/TASC.2009.2038717.

[9] C. C. Hwang, L. Y. Lyu, C. T. Liu, and P. L. Li, "Optimal design of an SPM motor using genetic algorithms and Taguchi method," in IEEE Transactions on Magnetics, 2008, vol. 44, no. 11 PART 2, pp. 4325–4328, doi: 10.1109/TMAG.2008.2001526.

[10] S. Nuzzo et al., "A Methodology to Remove Stator Skew in Small-Medium Size Synchronous Generators via Innovative Damper Cage Designs," IEEE Trans. Ind. Electron., vol. 66, no. 6, pp. 4296–4307, Jun. 2019, doi: 10.1109/TIE.2018.2864699.

[11] S. Nuzzo, M. Galea, C. Gerada, and N. Brown, "Analysis, Modeling, and Design Considerations for the Excitation Systems of Synchronous Generators," IEEE Trans. Ind. Electron., vol. 65, no. 4, pp. 2996–3007, Apr. 2018, doi: 10.1109/TIE.2017.2756592.

[12] M. Raza Khowja, C. Gerada, G. Vakil, P. Wheeler, and C. Patel, "Novel integrative options for passive filter inductor in high speed AC drives," in IECON Proceedings (Industrial Electronics Conference), 2016, vol. 0, pp. 1137–1142, doi: 10.1109/IECON.2016.7793661.

[13] M. R. Khowja, C. Gerada, G. Vakil, C. Patel, and P. Wheeler, "Design optimization of integrated rotor-less inductors for high-speed AC drive applications," in Proceedings - 2017 IEEE Workshop on Electrical Machines Design, Control and Diagnosis, WEMDCD 2017, 2017, pp. 69–74, doi: 10.1109/WEMDCD.2017.7947726.

[14] M. Raza Khowja, C. Gerada, G. Vakil, C. Patel, and P. Wheeler, "Design optimization of integrated rotational inductor for high-speed AC drive applications," in 2017 IEEE International Electric Machines and Drives Conference, IEMDC 2017, 2017, doi: 10.1109/IEMDC.2017.8002145.

[15] R. Ni, G. Wang, X. Gui, and D. Xu, "Investigation of d- and q-axis inductances influenced by slot-pole combinations based on axial flux permanent-magnet machines," IEEE Trans. Ind. Electron., vol. 61, no. 9, pp. 4539–4551, 2014, doi: 10.1109/TIE.2013.2288211.

[16] M. R. Khowja, G. Vakil, and C. Gerada, "Analytical Tool to Generate Torque-Speed Characteristics for Surface Mounted PM Machines in Constant Torque and Field Weakening Regions," in IECON Proceedings (Industrial Electronics Conference), 2019, vol. 2019-October, pp. 622–627, doi: 10.1109/IECON.2019.8927436.

[17] A. Bindra, "Wide-Bandgap Power Devices: Adoption Gathers Momentum," IEEE Power Electron. Mag., vol. 5, no. 1, pp. 22–27, 2018, doi: 10.1109/MPEL.2017.2782404.

[18] J. Umuhoza, H. Mhiesan, K. Mordi, C. Farnell, and H. Alan Mantooth, "Evaluation of 1.2 kV SiC MOSFETs in Modular Multilevel Cascaded H-Bridge Three-Phase Inverter for Medium Voltage Grid Applications," 2018 1st Work. Wide Bandgap Power Devices Appl. Asia, WiPDA Asia 2018, pp. 205–212, 2018, doi: 10.1109/WiPDAAsia.2018.8734536.

[19] Y. Shi, R. Xie, L. Wang, Y. Shi, and H. Li, "Switching Characterization and Short-Circuit Protection of 1200 v SiC MOSFET T-Type Module in PV Inverter Application," IEEE Trans. Ind. Electron., vol. 64, no. 11, pp. 9135–9143, Nov. 2017, doi: 10.1109/TIE.2017.2682800.

[20] C. Chen, Y. Chen, Y. Tan, J. Fang, F. Luo, and Y. Kang, "On the Practical Design of a High Power Density SiC Single-Phase Uninterrupted Power Supply System," IEEE Trans. Ind. Informatics, vol. 13, no. 5, pp. 2704–2716, Oct. 2017, doi: 10.1109/TII.2017.2677465.

[21] C. Chen, Y. Chen, Y. Li, Z. Huang, T. Liu, and Y. Kang, "An SiC-Based Half-Bridge Module with an Improved Hybrid Packaging Method for

High Power Density Applications," IEEE Trans. Ind. Electron., vol. 64, no. 11, pp. 8980–8991, Nov. 2017, doi: 10.1109/TIE.2017.2723873.
[22] K. Takao, S. Harada, T. Shinohe, and H. Ohashi, "Performance evaluation of all SiC power converters for realizing high power density of 50 W/cm3," in 2010 International Power Electronics Conference - ECCE Asia -, IPEC 2010, 2010, pp. 2128–2134, doi: 10.1109/IPEC.2010.5543727.
[23] J. Xu, D. Chen, and L. Spaziani, "A performance comparison of GaN E-HEMTs versus SiC MOSFETs in power switching applications," Bodo's Power Syst., pp. 36–39, 2017.
[24] Q. X. Guan et al., "An Extremely High Efficient Three-Level Active Neutral-Point-Clamped Converter Comprising SiC and Si Hybrid Power Stages," IEEE Trans. Power Electron., vol. 33, no. 10, pp. 8341–8352, Oct. 2018, doi: 10.1109/TPEL.2017.2784821.
[25] A. Nawawi et al., "Design and Demonstration of High Power Density Inverter for Aircraft Applications," IEEE Trans. Ind. Appl., vol. 53, no. 2, pp. 1168–1176, Mar. 2017, doi: 10.1109/TIA.2016.2623282.
[26] J. Brombach, M. Jordan, F. Grumm, and D. Schulz, "Converter topology analysis for aircraft application," SPEEDAM 2012 - 21st Int. Symp. Power Electron. Electr. Drives, Autom. Motion, pp. 446–451, 2012, doi: 10.1109/SPEEDAM.2012.6264483.
[27] R. Wu and G. R. Slemon, "A Permanent Magnet Motor Drive without a Shaft Sensor," IEEE Trans. Ind. Appl., vol. 27, no. 5, pp. 1005–1011, 1991, doi: 10.1109/28.90359.
[28] Z. Wang, K. Lu, and F. Blaabjerg, "A Simple Startup Strategy Based on Current Regulation for Back-EMF-Based Sensorless Control of PMSM," IEEE Trans. Power Electron., vol. 27, no. 8, pp. 3817–3825, Aug. 2012, doi: 10.1109/TPEL.2012.2186464.
[29] A. Ştirban, I. Boldea, G. D. Andreescu, D. Iles, and F. Blaabjerg, "Motion sensorless control of BLDC PM motor with offline FEM info assisted state observer," in Proceedings of the International Conference on Optimisation of Electrical and Electronic Equipment, OPTIM, 2010, pp. 321–328, doi: 10.1109/OPTIM.2010.5510439.
[30] M. Fatu, R. Teodorescu, I. Boldea, G. D. Andreescu, and F. Blaabjerg, "I-F starting method with smooth transition to EMF based motion-sensorless vector control of PM synchronous motor/generator," in PESC Record - IEEE Annual Power Electronics Specialists Conference, 2008, pp. 1481–1487, doi: 10.1109/PESC.2008.4592146.
[31] Y. Liang and Y. Li, "Sensorless control of PM synchronous motors based on MRAS method and initial position estimation," ICEMS 2003 - Proc. 6th Int. Conf. Electr. Mach. Syst., vol. 1, pp. 96–99, 2003.
[32] Young Sam Kim, Sang Kyoon Kim, and Young Ahn Kwon, "MRAS based sensorless control of permanent magnet synchronous motor," in SICE 2003 Annual Conference (IEEE Cat. No.03TH8734), 2003, vol. 2, pp. 1632-1637 Vol.2.
[33] B. Wuri Harini, A. Subiantoro, and F. Yusivar, "Stability of the Rotor Flux Oriented Speed Sensorless Permanent Magnet Synchronous Motor Control," in IEEE International Symposium on Industrial Electronics, 2018, vol. 2018-June, pp. 283–289, doi: 10.1109/ISIE.2018.8433862.
[34] C. Li, G. Wang, G. Zhang, N. Zhao, and Di. Xu, "Review of parameter identification and sensorless control methods for synchronous reluctance machines," Chinese J. Electr. Eng., vol. 6, no. 2, pp. 7–18, 2020, doi: 10.23919/CJEE.2020.000007.
[35] H. Kim, M. W. Degner, J. M. Guerrero, F. Briz, and R. D. Lorenz, "Discrete-time current regulator design for AC machine drives," IEEE Trans. Ind. Appl., vol. 46, no. 4, pp. 1425–1435, 2010, doi: 10.1109/TIA.2010.2049628.
[36] C. Li et al., "A Modified Neutral Point Balancing Space Vector Modulation for Three-Level Neutral Point Clamped Converters in High-Speed Drives," IEEE Trans. Ind. Electron., vol. 66, no. 2, pp. 910–921, Feb. 2019, doi: 10.1109/TIE.2018.2835372.
[37] G. B. Sugden, "Oil-cooled a.c. generators for aircraft —present trends," Students Q. J., vol. 40, no. 160, p. 128, 1970, doi: 10.1049/sqj.1970.0038.

Yuzheng Chen received the B.E. and M.E. degree in electrical engineering from Zhejiang University, China, in 2015 and 2018. He is currently working toward the Ph.D. degree in electrical engineering from the University of Nottingham, UK. His research interests include sensorless control, torque ripple suppression and flux weakening control on multi-phase permanent magnet machine.

Tao Yang (SM'20) received his MEng Degree from Shanghai Jiao Tong University, China in 2008 and his Ph.D. degree in electrical engineering from the University of Nottingham, UK in 2013.

Since 2013, he has been a Researcher with Power Electronics, Machines and Control Group, University of Nottingham, where he became an Assistant Professor in 2016, and an Associate Professor in 2019. His research interests include high-speed electric motor drive control, power electronic conversion, electrical system design and optimization for more electric/hybrid/all-electric aircraft applications. His PhD research within EU Clean Sky on "Modelling electrical power system for more-electric aircraft applications" has resulted in him winning the inaugural "Clean Sky Best PhD Award" in 2016. Dr. Yang is an Associate Editor for the IEEE Transactions on Transportation Electrification and Chinese Journal of Aeronautics.

Muhammad Raza Khowja received the B.Eng. (Hons) degree in Electrical Power Engineering from Mehran University of Engineering & Technology, Jamshoro, Pakistan, in 2011. He received his MSc degree in Electrical Engineering in 2012. He has received his PhD degree in Electrical & Electronics Engineering in 2018 from The University of Nottingham, UK where he is currently working as a Research Fellow in Power Electronics, Machines, and Control (PEMC) Group. His main research interest includes integrated passive components, design and development of high-performance electrical machines, characterisation and lifetime modelling of insulating materials.

Antonino La Rocca received his Ph.D. from the Department of Mechanical, Materials and Manufacturing Engineering Department, University of Nottingham, UK, in 2016. He is a Research Fellow in the Fluids and Thermal Engineering Research Group and the Power Electronics, Machines and Control Research Group in the Faculty of Engineering at the University of Nottingham. His research field is the thermo-mechanical modelling and design of high speed and high power dense electrical machines, power electronics and battery packs for advanced generation and propulsion systems by the use of Lumped Parameters Thermal networks (LPTN) and Computational Fluid Dynamics (CFD) and FEA.

Usman Nasir (S'13) received the B.Sc. degree in electrical engineering from the National University of Sciences and Technology, Islamabad, Pakistan, in 2013, and the M.Sc. degree in electric power system and its automation from North China Electric Power University, Beijing, China, in 2015. He got a PhD degree in Electrical Engineering with focus on power electronics converter design from The University of Nottingham, UK. He is currently associated with Compound Semiconductor Applications (CSA) Catapult, UK. His current research interests include wideband-gap devices e.g. SiC and GaN, new matrix converter-based topologies, novel

commutation and modulation techniques, thermal characterisation of devices and high-power density converters for automotive and aerospace applications.

Shajjad Chowdhury (Senior Member, IEEE) received the B.Sc. degree in electrical and electronics engineering from the American International University—Bangladesh, Dhaka, Bangladesh, in 2009, the M.Sc. degree in power and control engineering from Liverpool John Moores University, Liverpool, U.K., in 2011, and the Ph.D. degree in electrical and electronics engineering from the University of Nottingham, Nottingham, U.K., in 2016.

Thomas Klonowski received his MEng Degree from Institut National Polytechnique of Toulouse, ENSEEIHT, France in 2002 and his Ph.D. degree in electrical engineering from the University of Paris XI, France in 2006.

Since 2012, he has been hybrid-electric systems expert of mechatronics systems for aeronautics domains, Safran Helicopter Enignes. His research interests include compactness and fault tolerant high-speed electric motor drive control, power electronic conversion, electrical storage, electrical system design and optimization for more electric/hybrid/all-electric aircraft applications.

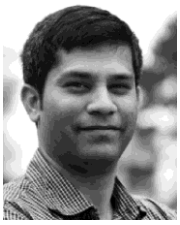

Gaurang Vakil (Member, IEEE) received the Ph.D. degree in variable speed generator design for renewable energy applications from the Power Electronics, Machines and Drives Group, IIT Delhi, New Delhi, India, in 2016. He subsequently worked as a Research Associate with the Power Electronics, Machines and Controls Group, University of Nottingham, Nottingham, U.K., where he was appointed as an Assistant Professor with the Department of Electrical and Electronics Engineering in 2016. His main research interests include design and development of high-performance electrical machines for transport and propulsion, optimizing electric drive-train for pure electric and hybrid vehicles (aerospace and automotive), high-power density machines, and magnetic material characterization.

Chris Gerada (Senior Member, IEEE) received the Ph.D. degree in numerical modelling of electrical machines from the University of Nottingham, Nottingham, U.K., in 2005. He subsequently worked as a Researcher with the University of Nottingham on high-performance electrical drives and on the design and modelling of electromagnetic actuators for aerospace applications. He was appointed a Lecturer in electrical machines in 2008, an Associate Professor in 2011, and Professor in 2013. His core research interests include the design and modelling of high-performance electric drives and machines. Prof. Gerada is an Associate Editor of the IEEE Transaction on Industry Applications. He has secured major industrial, European and U.K. grants, authored more than 200 papers and was awarded a Royal Academy of Engineering Research Chair to consolidate research in the field.

Serhiy Bozhko (Senior Member, IEEE) received the M.Sc. and Ph.D. degrees in electromechanical systems from the National Technical University of Ukraine, Kyiv City, Ukraine, in 1987 and 1994, respectively. Since 2000, he has been with the Power Electronics, Machines and Controls Research Group, University of Nottingham, U.K., where he is currently a Professor of aircraft electric power systems and the Director of the Institute for Aerospace Technology. He is leading several EU- and industry funded projects in the area of aircraft electric power systems, including power generation, distribution and conversion, power quality, control and stability issues, power management and optimization, as well as advanced modeling and simulations methods.

Christophe Diette, Technical coordinator in charge of roadmaps & partnerships. He graduated in Mechanical Engineering and received a PhD on Aerothermodynamics in turbomachinery at Von Karman Institute for Fluid Dynamics. He joined Safran Helicopter Engines in 2005 where he lead various engine projects, among them: the integration of the Adour turbofan engine into the nEUROn demonstrator for Unmanned Vehicle, the development & certification of the Arrius 2G1 turboshaft engine and the Clean Sky 2 Tech-TP turboprop engine demonstrator from 2014 to 2019. He joined Safran Aircraft Engines in 2019 in charge of the Clean Sky 2 programme and moved to the RISE programme early 2022.

Prof Pat Wheeler received his BEng [Hons] degree in 1990 from the University of Bristol, UK. He received his PhD degree in Electrical Engineering for his work on Matrix Converters from the University of Bristol, UK in 1994. In 1993 he moved to the University of Nottingham and worked as a research assistant in the Department of Electrical and Electronic Engineering. In 1996 he became a Lecturer in the Power Electronics, Machines and Control Group at the University of Nottingham, UK. Since January 2008 he has been a Full Professor in the same research group.

He was Head of the Department of Electrical and Electronic Engineering at the University of Nottingham from 2015 to 2018. He is currently the Head of the Power Electronics, Machines and Control Research Group, Global Director of the University of Nottingham's Institute of Aerosapce Technology and was the Li Dak Sum Chair Professor in Electrical and Aerospace Engineering. He is a member of the IEEE PELs AdCom and is currently IEEE PELS Vice-President for Technical Operations. He has published over 750 academic publications in leading international conferences and journals.